

Prediction of New Ground State Crystal Structure of Ta₂O₅

Yong Yang^{1*} and Yoshiyuki Kawazoe^{2,3}

1. *Key Laboratory of Materials Physics, Institute of Solid State Physics, Chinese Academy of Sciences, Hefei 230031, China.*
2. *New Industry Creation Hatchery Center (NICHe), Tohoku University, 6-6-4 Aoba, Aramaki, Aoba-ku, Sendai, Miyagi 980-8579, Japan.*
3. *Department of Physics and Nanotechnology, SRM University, Kattankulathur, 603203, TN, India.*

Tantalum pentoxide (Ta₂O₅) is a wide-gap semiconductor which has important technological applications. Despite the enormous efforts from both experimental and theoretical studies, the *ground state crystal structure* of Ta₂O₅ is not yet uniquely determined. Based on first-principles calculations in combination with evolutionary algorithm, we identify a triclinic phase of Ta₂O₅, which is energetically much more stable than any phases or structural models reported previously. Characterization of the static and dynamical properties of the new phase reveals the common features shared with previous metastable phases of Ta₂O₅. In particular, we show that the *d*-spacing of ~ 3.8 Å found in the X-ray diffraction (XRD) patterns of many previous experimental works, is actually the radius of the second Ta-Ta coordination shell as defined by radial distribution functions.

*Corresponding Author (wateratnanoscale@hotmail.com; yyang@theory.issp.ac.cn)

I. INTRODUCTION

As a versatile wide-gap semiconducting material, tantalum pentoxide (Ta_2O_5) has attracted a lot of interests of research in the past decades. The intrinsic excellent dielectric properties make Ta_2O_5 a good candidate material to replace SiO_2 as the insulating layer for advanced electronic devices such as non-volatile memories [1-5] and organic transistors [6, 7]. Owing to its high refractive index, Ta_2O_5 has applications in the coating material of optical devices [8, 9] and the instruments for ultraprecise measurement such as the Laser Interferometer Gravitational-wave Observatory (LIGO) [10-12]. In the detection and observation of gravitational waves made by LIGO [13], alternating thin layers of SiO_2 and Ta_2O_5 (doped with TiO_2) serve as mirror coatings for the test masses of the detectors [10-12]. Additionally, as a transition metal oxide, Ta_2O_5 also finds its place in other applications such as corrosion resistant coatings [14, 15] and catalyst for electro- and photocatalysis [16-19].

Previous experimental studies have established that, Ta_2O_5 undergoes a phase transition at $T \sim 1593$ K (1320 °C), from the low-temperature phase (L- Ta_2O_5) to the high-temperature phase (H- Ta_2O_5) [20]. In the research works that followed, many efforts are devoted to studying the crystallographic structures of both L- Ta_2O_5 and H- Ta_2O_5 , which still remain an issue of debate [21, 22]. Our work will focus on the atomic structures of the low-temperature phase of Ta_2O_5 , L- Ta_2O_5 , which is more relevant to technological applications. Due to the difficulties of growing high-quality single crystals of Ta_2O_5 , the structural information provided by powder X-ray diffraction (XRD) is very limited. Indeed, the crystal structures are found to be critically dependent on the conditions (e.g., temperatures, pressures) of synthesis and the method of analysis [23]. A number of phases and/or structural models have been suggested for L- Ta_2O_5 . Based on the data of powder XRD, Stephenson and Roth proposed the 11-formula-units ($Z = 11$, 22 Ta and 55 O atoms) orthorhombic model (referred to as L_{SR}) [24]. Later, the Hummel *et al.* proposed the T -phase (orthorhombic, space group: $Pmm2$) which is however nonstoichiometric in chemical components (unit cell contains 24 Ta and 62 O atoms) [21]. Grey, Mumme, and Roth

synthesized a new phase of L-Ta₂O₅ (referred to as L_{GMR}) whose unit cell is monoclinic with $Z = 19$ [25]. For the β -phase of L-Ta₂O₅, at least two different models with orthorhombic unit cells are found: the one (space group: *Pccm*) proposed by Aleshina and Loginova using Rietveld analysis of XRD pattern (referred to as β_{AL}) [26], and the one proposed by Ramprasad (referred to as β_R) [27], which is actually a simplified version of the L_{SR} model. Another orthorhombic phase, namely, the λ -model has been recently proposed with the space group *Pbam* [28]. The hexagonal unit cells of Ta₂O₅ are also reported by experimental works [21, 29]; however, the unit cell parameters and internal atomic coordinates of the phase are not fully determined until the work by Fukumoto and Miwa, which they called δ -Ta₂O₅ [30]. Two high-pressure phases, B-Ta₂O₅ (also known as ϵ -Ta₂O₅ [31]) and Z-Ta₂O₅ are synthesized at $P = 8$ GPa and $T = 1470$ K [32]. The B-Ta₂O₅ is found to be stable at atmospheric pressure and low temperatures. From the formation energies given by a recent work based on density functional theory (DFT) calculations [22], the stability of different phases of Ta₂O₅ is ranked in the order of $B > \lambda > L_{SR} > \beta_R > L_{GMR} > \delta > \beta_{AL}$. On the other hand, phonon calculations based on DFT show that the two β -phases (β_{AL} , β_R), and the δ -phase are dynamically unstable [22, 33].

In spite of these efforts, the *ground state crystal structure* of L-Ta₂O₅ is still elusive. Recent theoretical works based on the L_{SR} or the λ -phase have shown that, the ground state atomic structures of L-Ta₂O₅ can be energetically highly degenerated, and the creation of dilute oxygen vacancies can induce long-ranged perturbations on the atomic positions [34-36]. The concept of infinitely adaptive crystal structure [37] may account for such uncertainties or varieties of crystal structures, and leaves open the possibility of finding new phases/polymorphs of Ta₂O₅. In this work, we predict, based on *ab initio* evolutionary structure searches, a possible triclinic phase of Ta₂O₅, which is found to be more stable than any phases of Ta₂O₅ reported in literatures.

II. COMPUTATIONAL METHODS

Structure searches are performed using the *ab initio* evolutionary algorithm implemented in the USPEX package, which has demonstrated its reliability in

identifying new phases of bulk materials [38, 39]. The evolutionary simulations are carried out in the Ta₂O₅ systems whose unit cells contain two formula units ($Z = 2$). The first generation is produced randomly (119 structures), and the following generations are produced by heredity and lattice mutation (each generation contains 40 ~ 50 structures). Good convergence in the total energies is obtained after 19 generations (Fig. S1), surveying totally 1035 different crystal structures. During the structure search, all the local structural optimizations are done by the VASP code [40, 41], using a plane wave basis set and the projector-augmented-wave (PAW) potentials [42, 43], and uniform k-meshes with a spacing of $\sim 0.06 \times 2\pi \text{\AA}^{-1}$ for integration. The exchange-correlation interactions of electrons are described by the PBE type functional [44]. The energy cutoff for plane waves is 600 eV. The total energy of each configuration converges to a level of less than 1 meV/unit cell. After the evolutionary simulations, we analyzed the results by selecting a few of the lowest-energy structures (Generation 11 to 19) and optimized the unit cell and atomic structures again using VASP with a denser $10 \times 10 \times 4$ k-mesh, which ensures the total energy to converge to a level of less than 0.1 meV/unit cell. The set of the lowest-energy structures under consideration are well converged after re-optimization. The obtained new phase of Ta₂O₅ has a triclinic unit cell with the dimensional parameters (lengths and angles) as: $a = 3.89 \text{ \AA}$, $b = 3.89 \text{ \AA}$, $c = 13.38 \text{ \AA}$, $\alpha = 81.77^\circ$, $\beta = 98.25^\circ$, $\gamma = 89.67^\circ$, and space group $P1$ (atomic coordinates are provided in the Table SI). We have also optimized the structures of B, λ , L_{SR}, δ and β_{AL} phase of L-Ta₂O₅, and calculated their total energies using VASP to make a comparison with the new triclinic phase, which we call the γ phase hereafter for simplicity. The k-meshes for the calculations of B, λ , L_{SR}, δ and β_{AL} phase are $2 \times 4 \times 4$, $4 \times 4 \times 8$, $4 \times 2 \times 4$, $6 \times 6 \times 12$, $6 \times 12 \times 6$, respectively. All the k-meshes are generated by using the Monkhorst-Pack scheme [45]. The phonon dispersion and vibrational density of states (VDOS) of the γ phase are computed using the Quantum Espresso program [46], with the computational details provided in the Supplemental Material.

III. RESULTS AND DISCUSSION

A. Comparison with the previously identified phases of L-Ta₂O₅

The crystal structures of six phases of Ta₂O₅: β_{AL} , δ , L_{SR}, B, λ and γ are schematically shown in Fig. 1. Basically, the crystals of Ta₂O₅ are built up by a group of polyhedrons centered at Ta atoms with the vertexes of polyhedrons being O atoms [22, 27, 34]. From the number of O atoms that bonded with the central Ta, the polyhedrons can be classified into three types: octahedron (TaO₆), pentagonal bipyramid (TaO₇), and hexagonal bipyramid (TaO₈). The β_{AL} , B, λ and γ phase are solely formed by distorted octahedrons. The hexagonal δ phase is formed by edge-sharing octahedrons and hexagonal bipyramids, while the L_{SR} phase is constructed by edge and corner-sharing octahedrons and pentagonal bipyramids (Fig. 1). The optimized lattice parameters of the six Ta₂O₅ phases, the mass densities and their ground state energies with respect to the γ phase are tabulated in Table I. As expected, the PBE functional tends to overestimate the value of lattice parameters (by $\sim 4.8\%$ at most) while the PBEsol type functional [47] better describes the equilibrium geometries (error by $\sim 3.5\%$ at most, see Table SII). The PBE functional is chosen here for most calculations because it performs better than PBEsol in the calculation of energetic parameters [47, 48], which is our first concern for ranking the stability of different Ta₂O₅ phases. For the known Ta₂O₅ phases (β_{AL} , δ , L_{SR}, λ , B), the order of stability is found to be the same as previous studies [22]. To make a comparison, the relative energies of the optimized structures of the six phases calculated using the PBE [44], PBEsol [47], PW91 [49], HSE06 [50-52] and PBE0 [53] type functional are presented in Table I. It is clear that the γ -Ta₂O₅ stands as the most stable one for calculations using all the five types of functionals. Additionally, the first, second and third energetically favored phases, γ , B, and λ -Ta₂O₅, are built up only by octahedrons (TaO₆). This is in line with a recent qualitative analysis on B and λ -Ta₂O₅ [22]. For γ -Ta₂O₅, the band gap calculated by PBE functional is ~ 2.26 eV, and is increased to ~ 3.75 eV and 4.51 eV (Fig. S2), for calculations using the HSE06 [50-52] and PEB0 [53] type hybrid functionals, respectively. The band gap predicted by HSE06 is close to the value of λ -Ta₂O₅ (3.7 eV) [22, 28] but smaller than that of B-Ta₂O₅ (4.7 eV) [22]. The HSE06 band gaps of both λ and γ -Ta₂O₅ are comparable

with the experimental value, which is ~ 4 eV [54].

B. Possible pressure-induced phase transformation

The notable difference between the mass densities (Table I) of B, λ and γ -Ta₂O₅ implies that phase transformation may be induced by applied pressures. We firstly calculated the total energies E for a set of volumes V , and then deduced the analytic function $E(V)$ by least-squares fitting the E - V data to Murnaghan's equation of state

$$(EOS) [55, 56]: E(V) = \frac{B_0 V}{B_0'} \left[\left(\frac{V_0}{V} \right)^{\frac{B_0'}{B_0}} + 1 \right] + E(V_0) - \frac{B_0 V_0}{B_0' - 1},$$

where B_0 and B_0' are respectively the bulk modulus and its pressure derivative at equilibrium volume V_0 at which $E(V)$ reaches its minimum. The parameters B_0 and B_0' for the EOS of the three phases are listed in Table SIII. At $T = 0$ K, phase transformation occurs when the enthalpy $H = E + PV$ of two phases equals. It can be shown that pressure-induced phase transformation takes place along the common tangent line connecting the $E(V)$ curves of the two phases, with the transition pressure (P_t) given by negative value of the slope of the tangent line, and the corresponding transition volume (V_t) given by the point of tangency. The $E(V)$ curves and the tangent lines related to the phase transformation from γ -Ta₂O₅ to B and λ -Ta₂O₅ are shown in Fig. 2, and the transition pressures and volumes are listed in Table II. The transition pressure is ~ 1.78 GPa for the transformation from γ -Ta₂O₅ to B-Ta₂O₅, and is ~ 4.16 GPa for the transformation from γ -Ta₂O₅ to λ -Ta₂O₅. Experimentally, B-Ta₂O₅ was synthesized in a high-pressure chamber at $P = 8$ GPa and $T = 1470$ K [32]. Therefore, it is possible that in the initial stage of compression at lower pressure and temperature conditions, γ -Ta₂O₅ exists as a precursor phase prior transforming into the B phase. In the following studies, detailed comparison on the structural properties of these three phases will be presented.

C. Analysis of XRD patterns and radial distribution functions (RDF)

Figure 3(a) shows the simulated X-ray diffraction (XRD) pattern of γ -Ta₂O₅. The strongest reflection appears at the (010), (100), (011), and (10 $\bar{1}$) diffraction

planes with the incident angle 2θ varying from $\sim 23.11^\circ$ to 23.12° , and the d -spacing from $\sim 3.84 \text{ \AA}$ to 3.85 \AA . The smallest incident angle that produces a clear diffraction locates at $2\theta = 13.51^\circ$, with the index (002) and a d -spacing of $\sim 6.55 \text{ \AA}$, which is accordingly the largest separation between each pair of diffraction planes. The second and third strongest diffraction peaks are found at $2\theta = 33.26^\circ$, 27.21° ; with the d -spacing $\sim 2.70 \text{ \AA}$, 3.27 \AA , and the corresponding indexes (103), (004), respectively. As shown below, the strongest diffraction peak is associated with the second Ta-Ta coordination shell as defined by radial distribution function.

To study the dynamic arrangement of the neighboring atoms around Ta, the center of the TaO_6 octahedrons, we have performed *ab initio* molecular dynamics (MD) simulations at 300 K (detailed in Supplemental Texts) for γ , B, and λ - Ta_2O_5 , and calculated the radial distribution function (RDF) by averaging over all the atomic configurations involved within the simulation time. The calculated RDFs g_{TaO} and g_{TaTa} of γ - Ta_2O_5 are displayed in Figs. 3(b) and 3(c). The first and second RDF peaks of g_{TaO} (g_{TaTa}) correspond to the first and second Ta-O (Ta-Ta) atomic coordination shells, respectively. Broadening of the first peak of g_{TaO} corresponds the variation range of Ta-O bond lengths, whose averaged value ($\sim 2.00 \text{ \AA}$) is approximately at the peak position (R_{1P}), as indicated in Fig. 3(b). The geometric parameters associated with the RDFs of γ - Ta_2O_5 are listed in Table III, together with parameters related to the RDFs of B (Fig. S3) and λ - Ta_2O_5 (Fig. S4). Comparing the g_{TaO} of B and λ - Ta_2O_5 with γ - Ta_2O_5 , one sees that the averaged lengths of Ta-O bonds are all located at $\sim 2 \text{ \AA}$, in good agreement with available experimental data for TaO_6 octahedrons [24, 32].

For g_{TaTa} which describes the spatial distribution of TaO_6 octahedrons, the first and second peak of γ - Ta_2O_5 locates at $R_{1P} \sim 3.32 \text{ \AA}$ and $R_{2P} \sim 3.84 \text{ \AA}$, respectively. As found in Table III, the values of R_{1P} and R_{2P} of the three phases are close to each other: where the variation of R_{1P} and R_{2P} can be described by $R_{1P} \sim 3.30 \pm 0.02 \text{ \AA}$ and $R_{2P} \sim 3.80 \pm 0.08 \text{ \AA}$. The value of $R_{2P} \sim 3.80 \pm 0.08 \text{ \AA}$, is measured as one of the lattice parameters (c -axis) in a number of experimental studies on different Ta_2O_5 phases [21, 23-25, 29, 57, 58]. In the case of γ - Ta_2O_5 , it corresponds to the length of a -axis and b -axis. Therefore, the physical meaning of such a *characteristic length* is evident: It is

the radius of the second Ta-Ta coordination shells. Considering the fact that Ta atoms contain much more electrons than O atoms and consequently contribute dominantly to the XRD signals, it is natural to understand that it is the periodic arrangement of Ta atoms that determines the lattice parameters of Ta₂O₅. Indeed, this is supported by the XRD pattern shown in Fig. 3(a), in which the strongest diffraction is induced by a bundle of planes with the *d*-spacing of $\sim 3.84 \text{ \AA}$ to 3.85 \AA . Moreover, strong diffraction peaks at the corresponding incident angle $2\theta \sim 23^\circ$ under the Cu *K* α radiation (wave length $\lambda \sim 1.541 \text{ \AA}$) were observed in previous experimental measurements in different Ta₂O₅ polymorphs [18, 23, 31, 32, 59, 60]. The analysis above reveals that similar local atomic coordination structures are shared by different Ta₂O₅ polymorphs.

D. Comparison of the local bonding structures

The TaO₆ octahedrons constructing β , λ and γ -Ta₂O₅ are schematically shown in Figs. 4(a)-(c). Similarity of local Ta-O bonding structures is found in the Ta-O bond lengths, the surface areas and volumes of the octahedrons. The averaged Ta-O bond length is 2.02, 2.00, and 2.01 \AA ; the surface area is 27.78, 27.30, and 27.34 \AA^2 ; and the volume is 16.02, 15.24, and 15.52 \AA^3 , for β , λ and γ -Ta₂O₅, respectively. For each phase, the difference between the geometric parameters of every two octahedrons is found to be less than 1% and therefore can be regarded as the same. On the other hand, one can find the difference between the coordination O atoms, which can be divided into two types: the ones bonded with two Ta (referred to as O_{2c}), and the ones bonded with three Ta (referred to as O_{3c}). From the stoichiometry that every Ta is associated with 2.5 O atoms on average, one has the equalities: $n \times 1/3 + m \times 1/2 = 2.5$; $n + m = 6$, where n is the number of O_{3c} and m the number of O_{2c}. It follows that $n = m = 3$, which means that the number of the two types of O atoms are equal for the TaO₆ polyhedrons. On the other hand, the coordination structures of TaO₆ octahedrons of the three phases are distinct: Around the central Ta, there are six geometrically different O atoms in β -Ta₂O₅, while only five different O in λ -Ta₂O₅ and four different O in γ -Ta₂O₅. The six-coordination of λ and γ -Ta₂O₅ is achieved by periodic

extension of the crystal unit cells: the self-donated coordination O, i.e., the O “V” marked in Fig. 4(b) and O “I” and “IV” in Fig. 4(c). It is worthwhile to note here that, although the number of O_{2c} and O_{3c} is equal for the TaO_6 octahedron, the total number of O_{2c} and O_{3c} is different in the unit cell, whose ratio is 3:2 for the three phases.

Figures 4(d)-(f) show the neighboring octahedrons around an indicated TaO_6 octahedron, within the first and second Ta-Ta coordination shells as defined by g_{TaTa} [Fig. 3(c), Fig. S3(b), Fig. S4(b)]. The first and second coordination octahedrons are considered here due to the reasons: Firstly, the peak positions R_{1P} and R_{2P} only differ by $\sim 0.5 \text{ \AA}$ or less; and secondly, the boundary between the two coordination shells are flexible for B and λ - Ta_2O_5 , while only the sum of Ta-Ta coordination numbers (CNTa) of the two shells is invariant. The value of CNTa is 8 for both B and λ - Ta_2O_5 and is 7 for γ - Ta_2O_5 . The difference of CNTa originates from the positions of O_{3c} atoms as shown in Figs. 4(g)-(i). In principle, the maximum of CNTa that one TaO_6 can have is $n \times 2 + m \times 1 = 3 \times 2 + 3 \times 1 = 9$, by considering that one O_{3c} can contribute two neighboring Ta and one O_{2c} contribute one Ta at most. When two O_{3c} locate nearby and share one neighboring Ta with each other, as indicated in Figs. 4(g)-(h), the value of CNTa is reduced by one, i.e., CNTa = 8; when the three O_{3c} locate side-by-side as indicated in Fig. 4(i), CNTa is reduced by two, i.e., CNTa = 7. The smaller value of CNTa helps to understand the lower mass density of γ - Ta_2O_5 .

E. Analysis of Phonons

We go on to study the dynamical properties of γ - Ta_2O_5 by calculating the phonon spectrum based on density functional perturbation theory (DFPT) [61]. Compared to the direct method in which a large supercell may be employed [62], the DFPT method can study the phonon properties within the primitive cell. Figures 5(a)-(b) show the phonon dispersion along the Γ -X and Γ -L lines, and the vibrational density of states (VDOS) of phonons is shown in Fig. 5(c). The dynamical stability of γ - Ta_2O_5 is therefore confirmed by the absence of imaginary frequency points in the vibrational spectrum. Furthermore, the thermal stability of γ - Ta_2O_5 is also demonstrated by the regular and nearly equal-amplitude fluctuations of total energies

around a constant expected value as obtained by our MD simulations at 300 K (Fig. S5).

In previous works [59, 60, 63], the vibrational modes with the wavenumber $\tilde{\nu} > 800 \text{ cm}^{-1}$ are assigned to the internal Ta-O stretching motions of O_{2c} atoms, the modes at the region of $400 \text{ cm}^{-1} < \tilde{\nu} < 800 \text{ cm}^{-1}$ are assigned to the stretching motions of O_{3c} atoms, the modes at the region of $150 \text{ cm}^{-1} < \tilde{\nu} < 400 \text{ cm}^{-1}$ are attributed to the deformation motions of O_{2c} and O_{3c} with respect to the bonded Ta atoms, and the low frequency part $\tilde{\nu} < 150 \text{ cm}^{-1}$ are attributed to the external motions of TaO_n polyhedrons or Ta_xO_y clusters. We examine here the applicability of these assignments by studying the characteristics of vibrational modes of $\gamma\text{-Ta}_2\text{O}_5$ at the Γ -point (long-wavelength limit, VDOS shown in Fig. S6), which contribute majorly to the signals of Raman or infrared spectroscopy. The mode with the highest vibrational energy at Γ -point locates at $\tilde{\nu} = 1007 \text{ cm}^{-1}$ (Fig. S6), very close to the VDOS peak $\tilde{\nu} \sim 1009 \text{ cm}^{-1}$ indicated in Fig. 5(c). The polarization vector of this mode is shown in Fig. 5(d), which describes the direction and magnitude of atomic vibrations. It is clear that this mode is mainly due to the stretching motions of O_{2c} in the two neighboring TaO_6 , vibrating nearly along the c -axis with opposite directions. This is in line with the assignment of Raman spectroscopy measurement on the L_{SR} phase of Ta_2O_5 [60]. Correspondence with experiments is also found at the middle and low frequency part, for the vibrational modes at the Γ -point. The modes with $\tilde{\nu} \sim 510 \text{ cm}^{-1}$ and 570 cm^{-1} (Fig. S6) have been reported by measurements using Fourier-transform infrared spectroscopy (FTIR) on the thin films of Ta_2O_5 [63]. From their polarization vectors [Figs. S7(a)-(b)], these two modes are mainly associated with the vibrations of O_{3c} atoms. The mode with the wavenumber $\tilde{\nu} \sim 255 \text{ cm}^{-1}$ is recorded in the Raman spectra of different Ta_2O_5 phases [18, 59, 64]. In $\gamma\text{-Ta}_2\text{O}_5$, this mode is largely due to the vibrations of O_{2c} atoms along the c -axis, which leads to the bending of Ta-O-Ta bonds [Fig. S7(c)]. The lowest mode originating mainly from the vibrations of O_{2c} is located at the wavenumber $\tilde{\nu} \sim 91 \text{ cm}^{-1}$, which corresponds to the collective vibrations of O_{2c} along the b -axis [Fig. S7(d)]. For the vibrational modes with $\tilde{\nu} < 90 \text{ cm}^{-1}$, the motions of Ta atoms start to come into play. For instance, the two modes at

$\tilde{\nu} = 34 \text{ cm}^{-1}$, 35 cm^{-1} were reported in previous Raman spectroscopy measurements [59], which correspond to the collective vibrations of Ta and O atoms of γ -Ta₂O₅ (O_{2c} and O_{3c}) in the *ab* plane of the unit cell (Fig. S8). On the other hand, the vibrational spectrum of Ta₂O₅ can also be calculated by Fourier transform of the velocity autocorrelation function, which is readily deduced from the atomic trajectories recorded in MD simulations. Compared with the VDOS obtained by DFPT method, slight softening is observed in the Ta-O stretching modes of the vibrational spectrum (Fig. S9). This is mainly due to the different types of exchange-correlation functionals employed in the DFPT (Perdew-Zunger (abbr.: PZ) type, see Supplemental Texts) and MD simulations (PBE type), which lead to small difference in the optimized atomic structures and interatomic forces determined for vibrational frequency calculations. For instance, our DFPT calculations at Γ -point found that, the frequency of the highest and the second highest vibrational mode is $\sim 1007 \text{ cm}^{-1}$ and 910 cm^{-1} by PZ type functional, while it is $\sim 967 \text{ cm}^{-1}$ and 839 cm^{-1} by PBE type, respectively. Another reason may be the different temperatures considered for the system: 0 K in DFPT and 300 K in MD (mainly from Γ -point vibrations).

It should be noted here that the vibrational density of states is contributed from the phonons not only at Γ -point, but also at the other wave vectors (nonzero q-point) generated by the q-mesh employed in our DFPT calculations. Therefore, some of the vibrational modes at Γ -point appear as sides or shoulders of the peaks shown in Fig. 5(c). Nevertheless, comparison with the experimental data from different Ta₂O₅ polymorphs has demonstrated that, the common features shared by the local bonding structures (O_{2c}, O_{3c}) are reflected in some typical vibrational modes of the phonon spectra, despite the difference in mid- and long-range order which gives rises to different crystal structures. Indeed, previous measurements observed only minor difference between the Raman spectra of ceramic and crystalline Ta₂O₅ at room temperature [59]. Comparison with the RDFs calculated in amorphous Ta₂O₅ [65] also shows that, the upper limit of radii of the first and second Ta-O and Ta-Ta coordination shells in crystalline and amorphous Ta₂O₅ are approximately the same values.

Within the harmonic approximation, the vibrational contribution to the free energy can be written as [61] $F_{vib} = k_B T \sum_i \log\{2\sinh[\hbar\omega_i/(2k_B T)]\}$, where T is temperature, ω_i is phonon frequency, \hbar and k_B have the usual meanings. Under cryogenic conditions, the vibrational contribution to free energy is negligible. However, at temperatures well above 300 K, the entropy term due to atomic vibrations increases with elevating temperatures and therefore plays an important role in the total free energy of the system. As a result, the order of stability of different phases of Ta₂O₅ may change and the temperature-induced phase transition will take place. This is the topic of future research.

IV. CONCLUSIONS

In conclusion, using *ab initio* evolutionary algorithm, we report a possible new phase of Ta₂O₅ with triclinic unit cells. The triclinic phase is found to be more stable than any existing phases or structural models at low temperature. Detailed analysis and comparison with experimental data reveal that, common features present not only in the local bonding structures (e.g., the Ta-O bond lengths, the Ta and O local coordination structures, and the d -spacing ~ 3.8 Å in XRD pattern) of the triclinic phase and the other phases, but also in the dynamical properties such as the phonon spectra. Pressure-induced phase transformation is predicted to occur between the triclinic phase and the B and λ phase of Ta₂O₅ at pressures of several GPa. The results are expected to stimulate future experimental verifications and in-depth theoretical studies.

ACKNOWLEDGMENTS

We are grateful to the staff of the Hefei Branch of Supercomputing Center of Chinese Academy of Sciences; and the crew of Center for Computational Materials Science of the Institute for Materials Research, Tohoku University for their support of the SR16000 supercomputing facilities. We would like to thank Professor Wenguang Zhu for reading and helpful comments on the manuscript. Yong Yang acknowledges support from the National Natural Science Foundation of China (Grant No. 11474285).

References:

- [1] R. Waser, R. Dittmann, G. Staikov, and K. Szot, *Redox-Based Resistive Switching Memories – Nanoionic Mechanisms, Prospects, and Challenges*. *Adv. Mater.* **21**, 2632–2663 (2009).
- [2] C. Chaneliere, J. L. Autran, R. A. B. Devine, B. Balland, *Tantalum pentoxide (Ta_2O_5) thin films for advanced dielectric applications*. *Materials Science and Engineering*, **R22**, 269-322 (1998).
- [3] R. J. Cava, W. F. Peck, and J. J. Krajewski, *Enhancement of the dielectric constant of Ta_2O_5 through substitution with TiO_2* . *Nature* **377**, 215 (1995).
- [4] A. I. Kingon, J.-P. Maria and S. K. Streiffer, *Alternative dielectrics to silicon dioxide for memory and logic devices*. *Nature* **406**, 1032 (2000).
- [5] A. Wedig *et al.*, *Nanoscale cation motion in TaO_x , HfO_x and TiO_x memristive systems*. *Nat. Nanotech.* **11**, 67 (2015).
- [6] C. Bartic, H. Jansen, A. Campitelli, S. Borghs, *Ta_2O_5 as gate dielectric material for low-voltage organic thin-film transistors*. *Organic Electronics* **3**, 65–72 (2002).
- [7] A.-L. Deman, J. Tardy, *PMMA– Ta_2O_5 bilayer gate dielectric for low operating voltage organic FETs*. *Organic Electronics* **6**, 78–84 (2005).
- [8] H. O. Sankur and W. Gunning, *Deposition of optical thin films by pulsed laser assisted evaporation*. *Appl. Opt.* **28**, 2806 (1989).
- [9] T. J. Rehg, J. A. Ochoa-Tapia, A. Knoesen, and B. G. Higgins, *Solgel derived tantalum pentoxide films as ultraviolet antireflective coatings for silicon*. *Appl. Opt.* **28**, 5215 (1989).
- [10] D. R. M. Crooks *et al.*, *Excess mechanical loss associated with dielectric mirror coatings on test masses in interferometric gravitational wave detectors*. *Class. Quantum Grav.* **19**, 883–896 (2002).
- [11] G. M. Harry *et al.*, *Titania-doped tantala/silica coatings for gravitational-wave detection*. *Class. Quantum Grav.* **24**, 405–415 (2007).
- [12] G. M. Harry *et al.*, *Advanced LIGO: the next generation of gravitational wave detectors*. *Class. Quantum Grav.* **27**, 084006 (2010).
- [13] B. P. Abbott *et al.*, *Observation of Gravitational Waves from a Binary Black*

- Hole Merger*. Phys. Rev. Lett. **116**, 061102 (2016).
- [14] D. W. Graham and D. P. Stinton, *Development of Tantalum Pentoxide Coatings by Chemical Vapor Deposition*. J. Am. Ceram. Soc. **77**, 2298-2304 (1994).
- [15] P. M. Natishan, E. McCafferty, P. R. Puckett and S. Michel, *Ion Beam Assisted Deposited Tantalum Oxide Coatings on Aluminum*. Corrosion Science **38**, 1043-1049 (1996).
- [16] Yoshiro Ohgi *et al.*, *Oxygen reduction reaction on tantalum oxide-based catalysts prepared from TaC and TaN*. Electrochimica Acta **68**, 192– 197 (2012).
- [17] Z. Awaludin, T. Okajima, T. Ohsaka, *Preparation of reduced tantalum pentoxide by electrochemical technique for oxygen reduction reaction*. J. Power Sources **268**, 728-732 (2014).
- [18] Y. Zhu *et al.*, *Preparation and performances of nanosized Ta₂O₅ powder photocatalyst*. J. Solid State Chem. **178**, 224–229 (2005).
- [19] H. Sun, S. Liu, S. Liu, S. Wang, *A comparative study of reduced graphene oxide modified TiO₂, ZnO and Ta₂O₅ in visible light photocatalytic/photochemical oxidation of methylene blue*. Appl. Cat. B: Environ. **146**, 162– 168 (2014).
- [20] S. Lagergren and A. Magneli, *On the Tantalum-Oxygen System*. Acta Chem. Scand. **6**, 444 (1952).
- [21] H.-U. Hummel, R. Fackler, P. Remmert, *Tantaloxide durch Gasphasenhydrolyse, Druckhydrolyse und Transportreaktion aus 2H-TaS₅; Synthesen von TT-Ta₂O₅ und T-Ta₂O₅ und Kristallstruktur von T-Ta₂O₅*, Chem. Ber. **125**, 551 – 556 (1992).
- [22] S. Pérez-Walton, C. Valencia-Balvín, A. C. M. Padilha, G. M. Dalpian and J. M. Osorio-Guillén, *A search for the ground state structure and the phase stability of tantalum pentoxide*. J. Phys.: Condens. Matter **28**, 035801 (2016).
- [23] C. Askeljung, B.-O. Marinder, and M. Sundberg, *Effect of heat treatment on the structure of L-Ta₂O₅: a study by XRPD and HRTEM methods*. J. Solid State Chem. **176**, 250–258 (2003).
- [24] N. C. Stephenson and R. S. Roth, *Structural Systematics in the Binary System Ta₂O₅-WO₃. V. The Structure of the Low-Temperature Form of Tantalum Oxide L-Ta₂O₅*. Acta Cryst. **B27**, 1037 (1971).

- [25] I. E. Grey, W. G. Mumme, R. S. Roth, *The crystal chemistry of L-Ta₂O₅ and related structures*. J. Solid State Chem. **178**, 3308–3314 (2005).
- [26] L. A. Aleshina and S. V. Loginova, *Rietveld Analysis of X-ray Diffraction Pattern From β -Ta₂O₅ Oxide*. Crystallogr. Rep. **47**, 415–419 (2002).
- [27] R. Ramprasad, *First principles study of oxygen vacancy defects in tantalum pentoxide*. J. Appl. Phys. **94**, 5609 (2003).
- [28] S.-H. Lee, J. Kim, S.-J. Kim, S. Kim, and G.-S. Park, *Hidden Structural Order in Orthorhombic Ta₂O₅*. Phys. Rev. Lett. **110**, 235502 (2013).
- [29] N. Terao, *Structure des Oxydes de Tantale*. Jpn. J. Appl. Phys. **6**, 21 (1967).
- [30] A. Fukumoto and K. Miwa, *Prediction of hexagonal Ta₂O₅ structure by first-principles calculations*. Phys. Rev. B **55**, 11155 (1997).
- [31] F. Izumi and H. Kodama, *A new modification of tantalum (V) oxide*. J. Less-Common Met. **63**, 305-307 (1979).
- [32] I. P. Zibrov, V. P. Filonenko, M. Sundberg and P.-E. Werner, *Structures and phase transitions of B-Ta₂O₅ and Z-Ta₂O₅: two high-pressure forms of Ta₂O₅*. Acta Cryst. **B56**, 659-665 (2000).
- [33] W. Andreoni and C. A. Pignedoli, *Ta₂O₅ polymorphs: Structural motifs and dielectric constant from first principles*. Appl. Phys. Lett. **96**, 062901 (2010).
- [34] Y. Yang, H. Nahm, O. Sugino and T. Ohno, *Electronic structures of oxygen-deficient Ta₂O₅*. AIP Adv. **3**, 042101–9 (2013).
- [35] Y. Yang, O. Sugino, Y. Kawazoe, *Exceptionally long-ranged lattice relaxation in oxygen-deficient Ta₂O₅*. Solid State Commun. **195**, 16–20 (2014).
- [36] Y. Guo and J. Robertson, *Oxygen vacancy defects in Ta₂O₅ showing long-range atomic re-arrangements*. Appl. Phys. Lett. **104**, 112906 (2014).
- [37] J. S. Anderson, *On Infinitely Adaptive Structures*. J. Chem. Soc. Dalton Trans. **1973**, 1107 (1973).
- [38] A. R. Oganov and C. W. Glass, *Crystal structure prediction using ab initio evolutionary techniques: Principles and applications*. J. Chem. Phys. **124**, 244704-244716 (2006).
- [39] Q. Zhu, L. Li, A. R. Oganov, and P. B. Allen, *Evolutionary method for*

- predicting surface reconstructions with variable stoichiometry.* Phys. Rev. B **87**, 195317 (2013).
- [40] G. Kresse, J. Hafner, *Ab initio molecular dynamics for liquid metals.* Phys. Rev. B **47**, 558 (1993).
- [41] G. Kresse, J. Furthmüller, *Efficient iterative schemes for ab initio total-energy calculations using a plane-wave basis set.* Phys. Rev. B **54**, 11169 (1996).
- [42] P. E. Blöchl, *Projector augmented-wave method.* Phys. Rev. B. **50**, 17953 (1994).
- [43] G. Kresse, D. Joubert, *From ultrasoft pseudopotentials to the projector augmented-wave method.* Phys. Rev. B. **59**, 1758 (1999).
- [44] J. P. Perdew, K. Burke, M. Ernzerhof, *Generalized Gradient Approximation Made Simple.* Phys. Rev. Lett. **77**, 3865 (1996).
- [45] H. J. Monkhorst, J. D. Pack, *Special points for Brillouin-zone integrations.* Phys. Rev. B **13**, 5188 (1976).
- [46] P. Giannozzi *et al.*, *Quantum ESPRESSO: a modular and open-source software project for quantum simulations of materials.* J. Phys.: Condens. Matter **21**, 395502 (2009). Program web site: <http://www.quantum-espresso.org/>.
- [47] J. P. Perdew *et al.*, *Restoring the Density-Gradient Expansion for Exchange in Solids and Surfaces.* Phys. Rev. Lett. **100**, 136406 (2008).
- [48] R. Koitz *et al.*, *Scalable properties of metal clusters: A comparative study of modern exchange-correlation functionals.* J. Chem. Phys. **137**, 034102 (2012).
- [49] J. P. Perdew and Y. Wang, *Accurate and simple analytic representation of the electron-gas correlation energy.* Phys. Rev. B **45**, 13244 (1992).
- [50] J. Heyd, G. E. Scuseria, and M. Ernzerhof, *Hybrid functionals based on a screened Coulomb potential.* J. Chem. Phys. **118**, 8207 (2003).
- [51] J. Heyd and G. E. Scuseria, *Efficient hybrid density functional calculations in solids: Assessment of the Heyd–Scuseria–Ernzerhof screened Coulomb hybrid functional.* J. Chem. Phys. **121**, 1187 (2004).
- [52] J. Heyd, G. E. Scuseria, and M. Ernzerhof, *Erratum: “Hybrid functionals based on a screened Coulomb potential” [J. Chem. Phys. 118, 8207 (2003)].* J. Chem. Phys. **124**, 219906 (2006).

- [53] J. P. Perdew, M. Ernzerhof, and K. Burke, *Rationale for mixing exact exchange with density functional approximations*. J. Chem. Phys. **105**, 9982 (1996).
- [54] R. M. Fleming *et al.*, *Defect dominated charge transport in amorphous thin films*. J. Appl. Phys. **88**, 850 (2000).
- [55] F. D. Murnaghan, *The Compressibility of Media under Extreme Pressures*. Proc. Nat. Acad. Sci. **30**, 244 (1944).
- [56] https://en.wikipedia.org/wiki/Murnaghan_equation_of_state.
- [57] L. D. Calvert and P. H. G. Draper, *A Proposed Structure for Annealed Anodic Oxide Films of Tantalum*. Can. J. Chem. **40**, 1943 (1962).
- [58] K. Lehovec, *Lattice structure of β -Ta₂O₅*. J. Less-Common Met. **7**, 397 (1964).
- [59] P. S. Dobal, R. S. Katiyar, Y. Jiang, R. Guo and A. S. Bhalla, *Raman scattering study of a phase transition in tantalum pentoxide*. J. Raman Spectrosc. **31**, 1061–1065 (2000).
- [60] C. Joseph, P. Bourson and M. D. Fontana, *Amorphous to crystalline transformation in Ta₂O₅ studied by Raman spectroscopy*. J. Raman Spectrosc. **43**, 1146–1150 (2012).
- [61] S. Baroni, S. de Gironcoli, A. Dal Corso and P. Giannozzi, *Phonons and related crystal properties from density-functional perturbation theory*. Rev. Mod. Phys. **73**, 515 (2001).
- [62] K. Parlinski, Z. Q. Li and Y. Kawazoe, *First-principle determination of the soft mode in cubic ZrO₂*. Phys. Rev. Lett. **78**, 4063 (1997).
- [63] H. Ono, Y. Hosokawa, K. Shinoda, K. Koyanagi, H. Yamaguchi, *Ta-O phonon peaks in tantalum oxide films on Si*. Thin Solid Films **381**, 57-61 (2001).
- [64] J. F. Meng, B. K. Rai, R. S. Katiyar and A. S. Bhalla, *Raman Investigation on (Ta₂O₅)_{1-x}(TiO₂)_x System at Different Temperatures and Pressures*. J. Phys. Chem. Solids **58**, 1503-1506 (1997).
- [65] Y.-N. Wu, L. Li, and H.-P. Cheng, *First-principles studies of Ta₂O₅ polymorphs*. Phys. Rev. B **83**, 144105 (2011).

TABLE I. Calculated lattice and energetic parameters of the six Ta₂O₅ phases, where α, β, γ are the angles between the cell edges b and c , a and c , and a and b , respectively. Z is the number of Ta₂O₅ units in the unit cell, and ρ is mass density. The available experimental data (with the subscript expt) of cell lengths are listed for comparison. ΔE is ground state energy difference (per formula unit) relative to the γ phase, calculated using the PBE, PBEsol, PW91, HSE06 and PBE0 type exchange-correlation functionals. Due to the extremely heavy computational burden, the k-meshes employed in the HSE06 and PBE0 type hybrid functional calculations are $8 \times 8 \times 2$, $2 \times 4 \times 4$, $4 \times 4 \times 8$, $4 \times 2 \times 4$, $4 \times 4 \times 8$, and $4 \times 6 \times 4$, for the γ , B, λ , L_{SR}, δ and β_{AL} phase, respectively.

	β_{AL}	δ	L _{SR}	λ	B	γ	
a (Å)	6.52	7.33	6.33	6.25	12.93	3.89	
a_{expt} (Å)	^a 6.217	--	^b 6.198	--	^c 12.7853	--	
b (Å)	3.69	7.33	40.92	7.40	4.92	3.89	
b_{expt} (Å)	^a 3.677	--	^b 40.290	--	^c 4.8537	--	
c (Å)	7.78	3.89	3.85	3.82	5.59	13.38	
c_{expt} (Å)	^a 7.794	--	^b 3.888	--	^c 5.5276	--	
α (°)	90	90	90	90	90	81.77	
β (°)	90	90	90	90	103.23	98.25	
γ (°)	90	120	89.16	90	90	89.67	
Z	2	2	11	2	4	2	
ρ (g/cm ³)	7.85	8.12	8.10	8.29	8.48	7.42	
ΔE (eV/Ta ₂ O ₅)	PBE	2.326	1.966	0.309	0.243	0.117	0
	PBEsol	2.350	1.906	0.240	0.157	0.030	0
	PW91	2.342	1.977	0.320	0.253	0.126	0
	HSE06	2.444	2.053	0.214	0.220	0.101	0
	PBE0	2.506	2.042	0.273	0.207	0.018	0

^aExpt. [26]; ^bExpt. [24]; ^cExpt. [32].

TABLE II. Calculated transition volumes (V_t^γ , V_t^B , V_t^λ) and the transition pressures of Ta₂O₅ from the γ phase to B and λ phase.

	V_t^γ ($\text{\AA}^3/\text{f.u.}$)	V_t^B ($\text{\AA}^3/\text{f.u.}$)	V_t^λ ($\text{\AA}^3/\text{f.u.}$)	P_t (GPa)
$\gamma \rightarrow B$	98.08	85.46	---	1.78
$\gamma \rightarrow \lambda$	97.03	---	86.53	4.16

TABLE III. Geometric parameters describing the radial distribution functions (RDFs) of the λ , B, and γ -Ta₂O₅, which are obtained from MD simulations at 300 K (detailed in Supplemental Material). In the case of g_{TaO} , the radii $R_{1\text{L}}$ ($R_{2\text{L}}$), $R_{1\text{U}}$ ($R_{2\text{U}}$), and $R_{1\text{P}}$ ($R_{2\text{P}}$) are the lower limit, upper limit and the highest RDF peak positions defining the first (second) coordination shell, respectively. Similar convention applies to the RDF g_{TaTa} .

Radii of coordination shells	g_{TaO}			g_{TaTa}		
	λ	B	γ	λ	B	γ
$R_{1\text{L}}$ (Å)	1.72	1.68	1.72	3.08	3.10	3.10
$R_{1\text{U}}$ (Å)	2.50	2.52	2.56	3.44	3.44	3.58
$R_{1\text{P}}$ (Å)	1.92	1.96	1.94	3.28	3.32	3.32
$R_{2\text{L}}$ (Å)	2.50	3.10	3.38	3.44	3.44	3.64
$R_{2\text{U}}$ (Å)	3.50	3.74	4.02	4.06	4.06	4.12
$R_{2\text{P}}$ (Å)	3.10	3.56	3.86	3.80	3.72	3.84

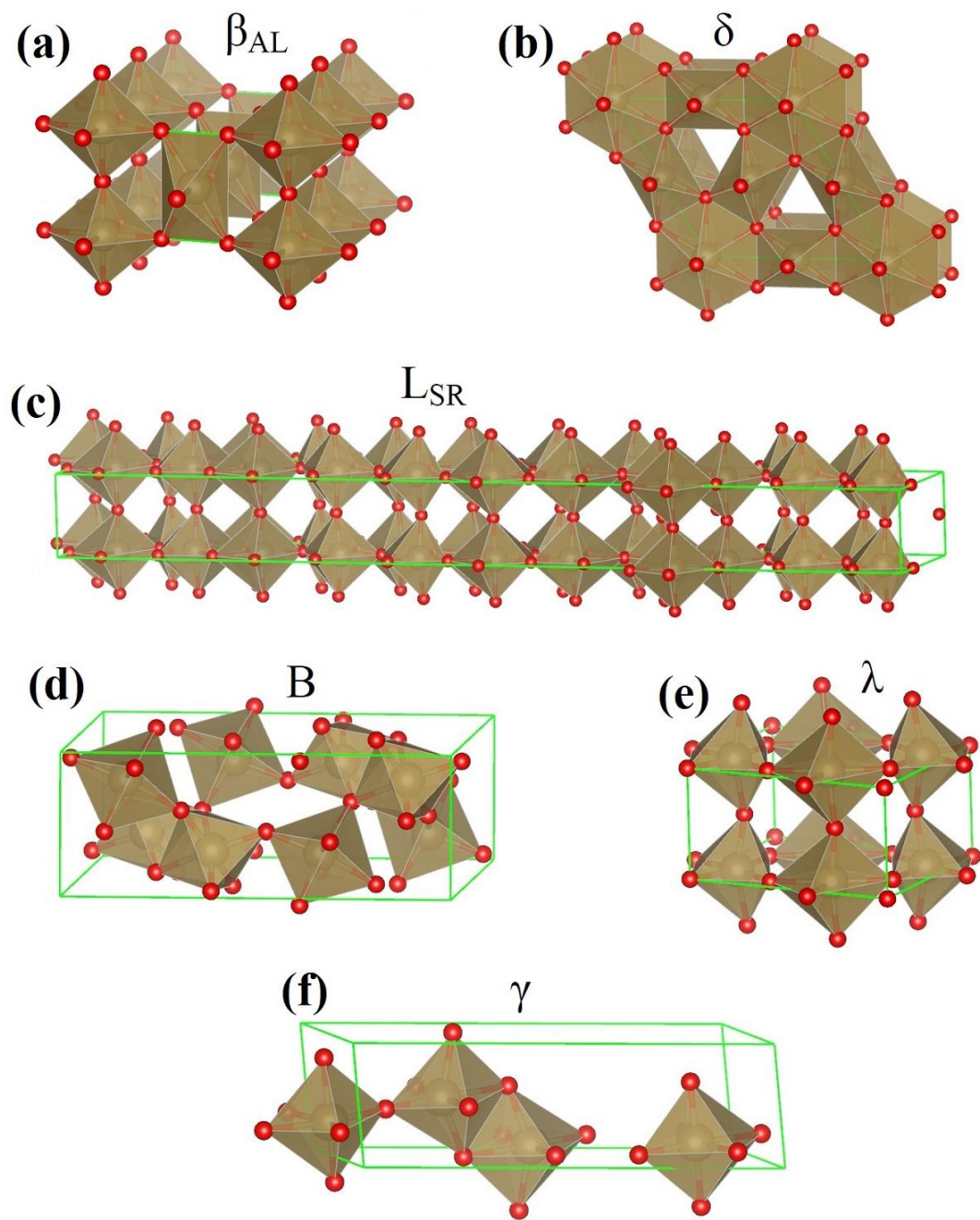


FIG. 1. Schematic diagram for the structural models of Ta₂O₅: (a) β_{AL} ; (b) δ ; (c) L_{SR} ; (d) B; (e) λ and (f) γ -Ta₂O₅.

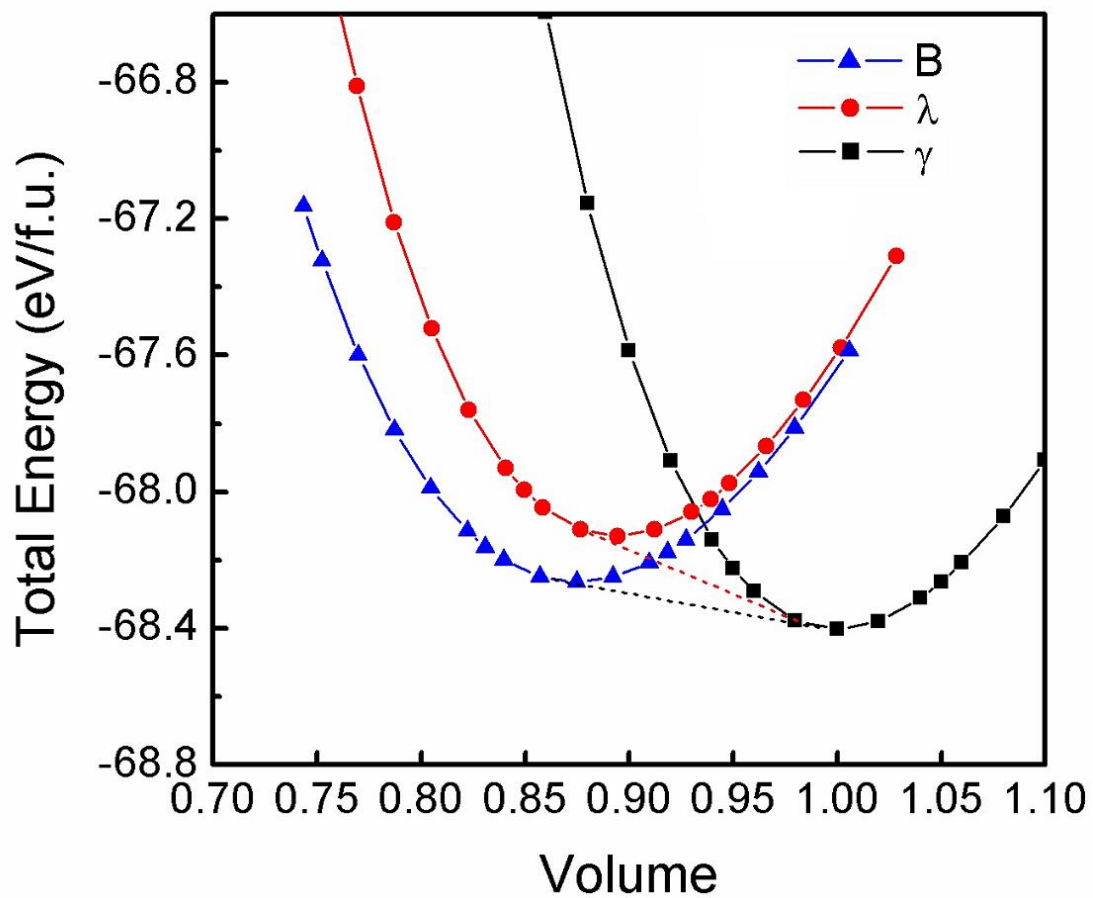


FIG. 2. Total energies of the B, λ and γ -Ta₂O₅ as a function of volumes normalized to the equilibrium volume of γ -Ta₂O₅ at $P = 0$ GPa. The dashed lines are common tangent along which phase transformation between two phases occurs.

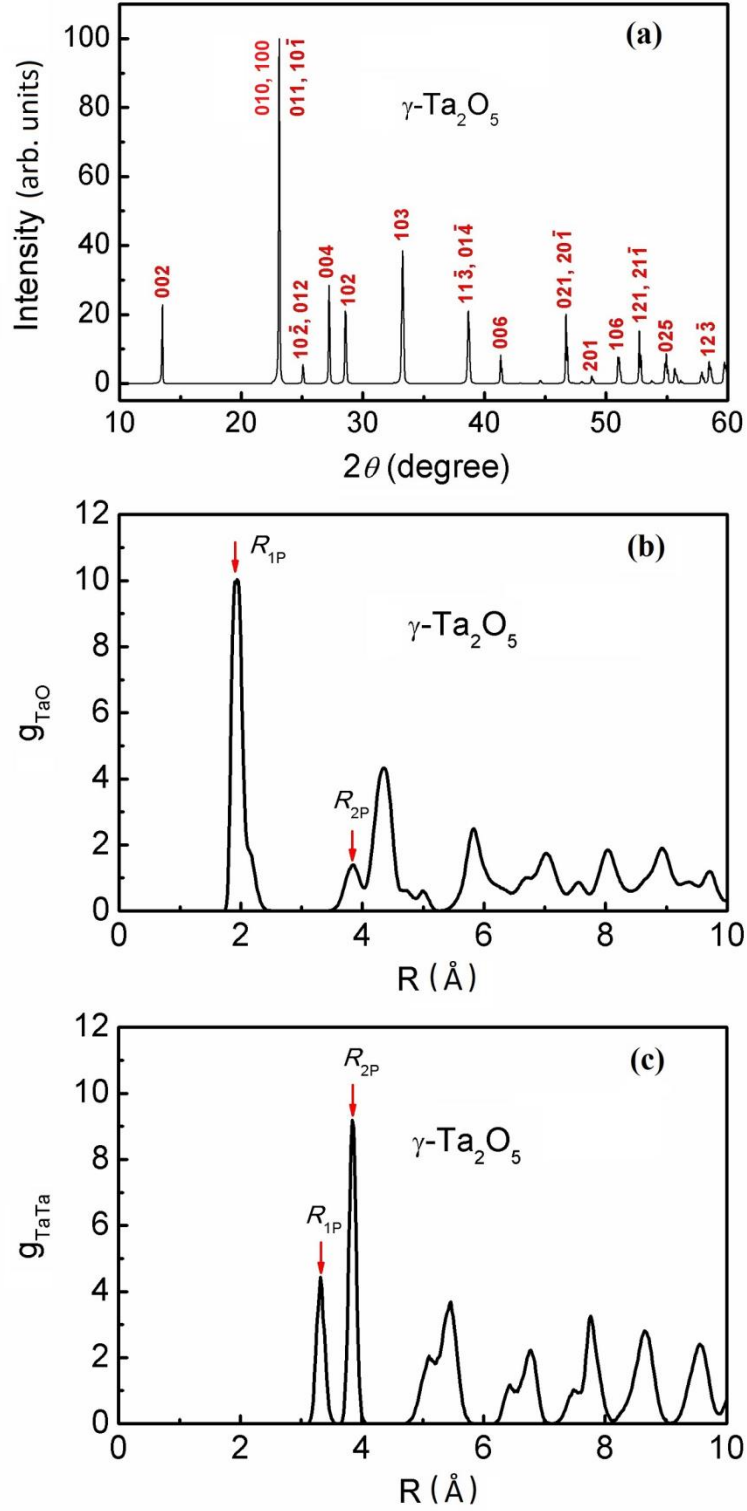


FIG. 3. (a) Simulated X-ray diffraction (XRD) pattern for γ -Ta₂O₅, using the Cu $K\alpha$ radiation (wave length $\sim 1.541 \text{ \AA}$). (b) – (c): The radial distribution functions (RDFs) g_{TaO} (b) and g_{TaTa} (c) of γ -Ta₂O₅, calculated by averaging over the atomic configurations obtained in MD simulations at 300 K.

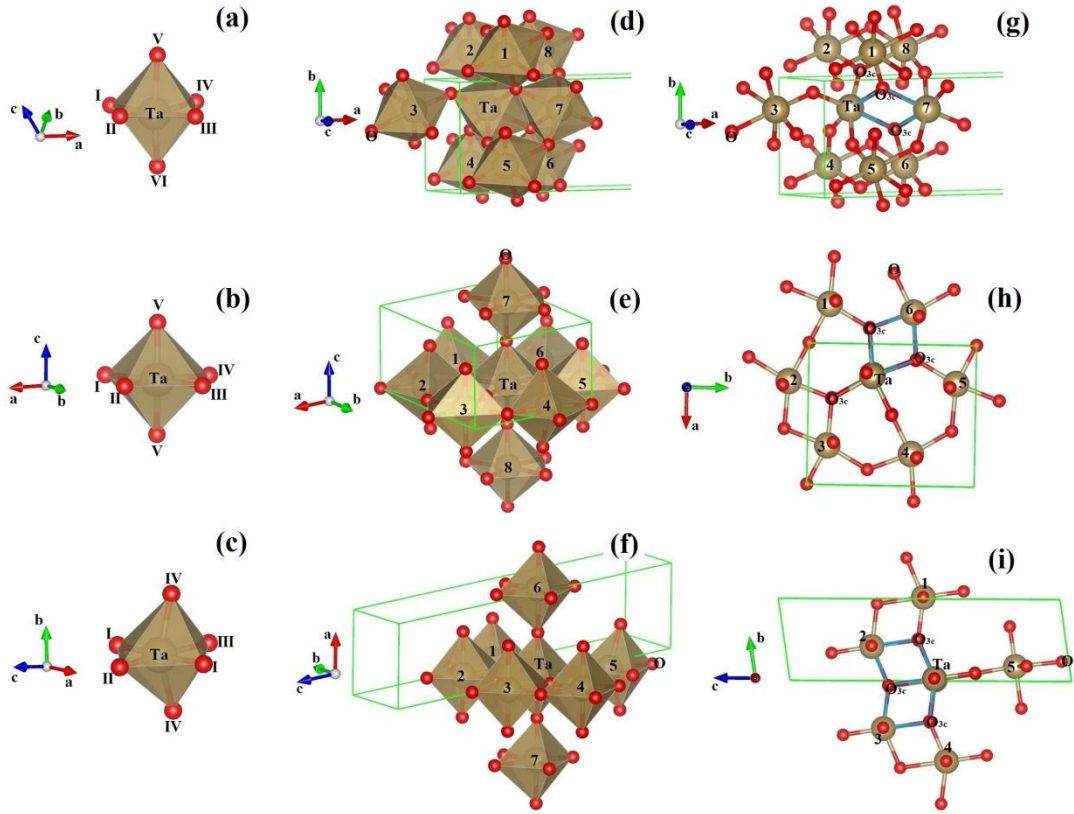


FIG. 4. The ball-and-stick representation of TaO_6 octahedrons (left panels), their spatial distribution around one central TaO_6 (middle panels), and the local bonding structures of O_{3c} (right panels) in B (**a, d, g**), λ (**b, e, h**), and $\gamma\text{-Ta}_2\text{O}_5$ (**c, f, i**).

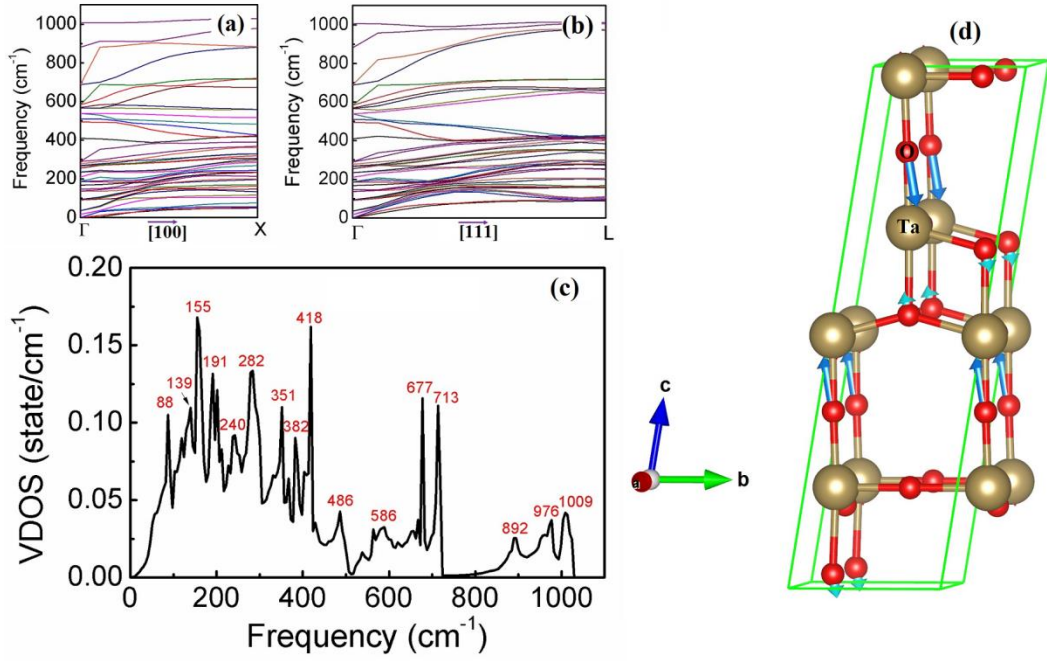


FIG. 5. Panels (a)-(c): Calculated phonon dispersions of γ -Ta₂O₅ along the Γ X (a) and Γ L (b) lines; and the vibrational density of states (VDOS, panel c). Panel (d): Polarization vectors of the vibrational modes of γ -Ta₂O₅ at Γ -point with the wave numbers $\tilde{\nu} = 1007 \text{ cm}^{-1}$. The vibrations of O_{3c} and O_{2c} are represented by sky-blue and deep-blue arrows, respectively.

Supplemental Material for “Prediction of New Ground State Crystal Structure of Ta₂O₅”

Yong Yang^{1*} and Yoshiyuki Kawazoe^{2,3}

1. *Key Laboratory of Materials Physics, Institute of Solid State Physics, Chinese Academy of Sciences, Hefei 230031, China.*
2. *New Industry Creation Hatchery Center (NICHe), Tohoku University, 6-6-4 Aoba, Aramaki, Aoba-ku, Sendai, Miyagi 980-8579, Japan.*
3. *Department of Physics and Nanotechnology, SRM University, Kattankulathur, 603203, TN, India.*

Contents:

- I. Supplemental Texts
- II. Supplemental Tables SI to SIII
- III. Supplemental Figs. S1 to S9
- IV. References

*E-mail: wateratnanoscale@hotmail.com; yyang@theory.issp.ac.cn

I. Supplemental Texts

A. Phonon calculations using Quantum Espresso

Phonon dispersion and vibrational density of states (VDOS) were calculated using Quantum Espresso (QE) package, where the unit cell geometry and atomic structures are fully re-optimized from the results obtained by VASP code [40, 41]. The wave function of valence electrons is expanded using a plane-wave basis set with a kinetic energy cut-off of 75 Ry. The ion-electron interactions are described by the PAW methods [42, 43], and the exchange-correlation energies are described using the Perdew-Zunger functional [66]. For the calculation of the electronic wave function, the Brillouin zone (BZ) is sampled using a $10 \times 10 \times 4$ Monkhorst-Pack k-mesh [45]. The Gaussian smearing is employed for doing integration in the Brillouin-zone, with a smearing parameter of 0.05 Ry. A $8 \times 8 \times 2$ uniform q -point grid is used for the calculation of dynamical matrices, which are then diagonalized to get the eigen-frequency $\omega(q)$ (q : wave vector). The dynamical matrices of denser q -meshes can be obtained by using interpolation method and Fourier transform to get the force constants in real space.

After the structural re-optimization using QE package, the obtained unit cell parameters are as follows: $a = 3.82 \text{ \AA}$, $b = 3.82 \text{ \AA}$, $c = 13.13 \text{ \AA}$, $\alpha = 81.71^\circ$, $\beta = 98.29^\circ$, $\gamma = 90.00^\circ$. The unit cell is slightly contracted, and the averaged Ta-O bond length decreases from $\sim 2.00 \text{ \AA}$ (by VASP) to $\sim 1.97 \text{ \AA}$ (by QE).

B. MD simulations using VASP code

To check the thermal stability of γ -Ta₂O₅, first-principles molecular dynamics (MD) simulations were performed at 300 K in a system modeled by the $(4 \times 4 \times 2)$ supercell of γ -Ta₂O₅, which contains 448 atoms. A canonical ensemble is simulated using the algorithm of Nosé [67-69]. The dynamics of the system are simulated for ~ 2 ps.

MD simulations at 300 K are also performed for B and λ phase of Ta₂O₅, in a canonical ensemble for ~ 2 ps, to calculate the averaged radial distribution functions

(RDFs) and make a comparison with γ -Ta₂O₅. A (2×4×3) and (3×3×4) supercell is employed for the simulations of B and λ -Ta₂O₅, respectively.

For the three simulated systems, the minimum of the lengths of the supercell axis are larger than 15 Å. In all the MD simulations, the time step is 0.5 fs; and only the Γ -point is used for total energy calculations, due to the very large size of simulation systems and consequently much small size of BZ for integration.

II. Supplemental Tables: TABLE SI to TABLE SIII

TABLE SI. Atomic coordinates of γ -Ta₂O₅ from first-principles calculations, in units of Å.

Atom	X	Y	Z
Ta1	-1.20282	1.39956	9.40698
Ta2	2.96610	0.54107	2.77774
Ta3	-1.00656	-0.04931	6.40177
Ta4	-1.26833	0.64726	13.16289
O1	0.88804	-0.11769	6.46959
O2	-1.03289	1.77626	7.24990
O3	3.05393	0.83464	0.60284
O4	2.89698	0.15715	4.65301
O5	-1.06570	3.40826	9.22737
O6	1.04384	0.63679	2.18186
O7	3.01652	2.40860	3.10127
O8	0.78716	1.35444	9.47984
O9	-1.21954	1.03758	11.28834
O10	-1.19216	2.60923	13.50713

TABLE II. Lattice parameters (unit cell lengths a , b and c) of the six Ta₂O₅ phases, calculated using the PBEsol and PW91 exchange-correlation functional (labeled by subscripts). The experimental data are listed for comparison.

	β_{AL}	δ	L_{SR}	λ	B	γ
$a_{\text{PBEsol}} (\text{\AA})$	6.44	7.27	6.29	6.21	12.85	3.87
$a_{\text{PW91}} (\text{\AA})$	6.51	7.33	6.34	6.25	12.93	3.88
$a_{\text{expt}} (\text{\AA})$	^a 6.217	--	^b 6.198	--	^c 12.7853	--
$b_{\text{PBEsol}} (\text{\AA})$	3.68	7.27	40.56	7.34	4.87	3.87
$b_{\text{PW91}} (\text{\AA})$	3.69	7.33	40.91	7.40	4.93	3.89
$b_{\text{expt}} (\text{\AA})$	^a 3.677	--	^b 40.290	--	^c 4.8537	--
$c_{\text{PBEsol}} (\text{\AA})$	7.74	3.87	3.83	3.80	5.53	13.30
$c_{\text{PW91}} (\text{\AA})$	7.77	3.89	3.84	3.83	5.59	13.34
$c_{\text{expt}} (\text{\AA})$	^a 7.794	--	^b 3.888	--	^c 5.5276	--

^aExpt. [26]; ^bExpt. [24]; ^cExpt. [32].

TABLE III. The bulk modulus and its pressure derivative in Murnaghan's equation of state (EOS), calculated for λ , B and γ -Ta₂O₅.

	λ	B	γ
B_0 (GPa)	175.0	138.6	201
B'	5.3	3.8	6.43

III. Supplemental Figures: FIG. S1 to FIG. S9

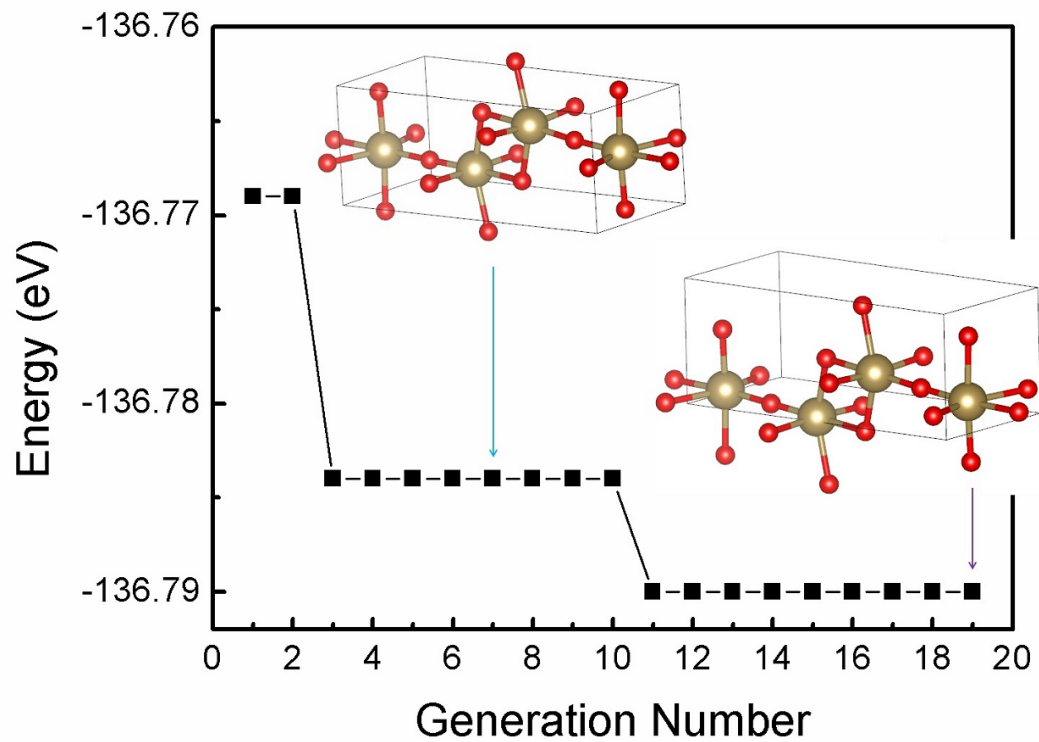


FIG. S1. Total energy of the best Ta₂O₅ structure as function of generation number predicted by USPEX.

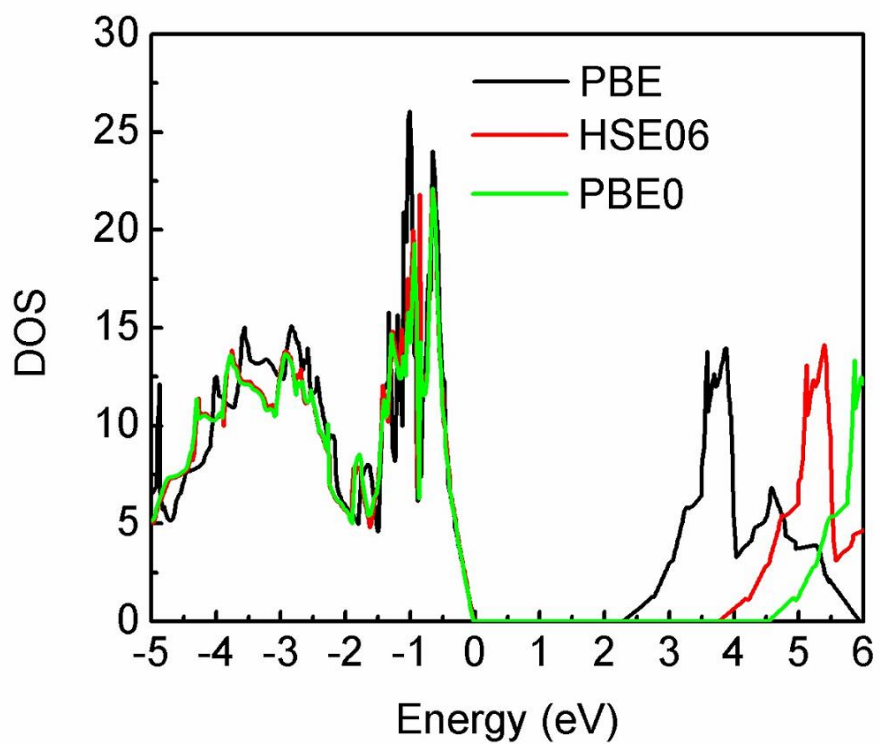


FIG. S2. Calculated electron density of states (DOS) of γ -Ta₂O₅ using the PBE, HSE06 and PBE0 type functionals. The Fermi level is set at 0.

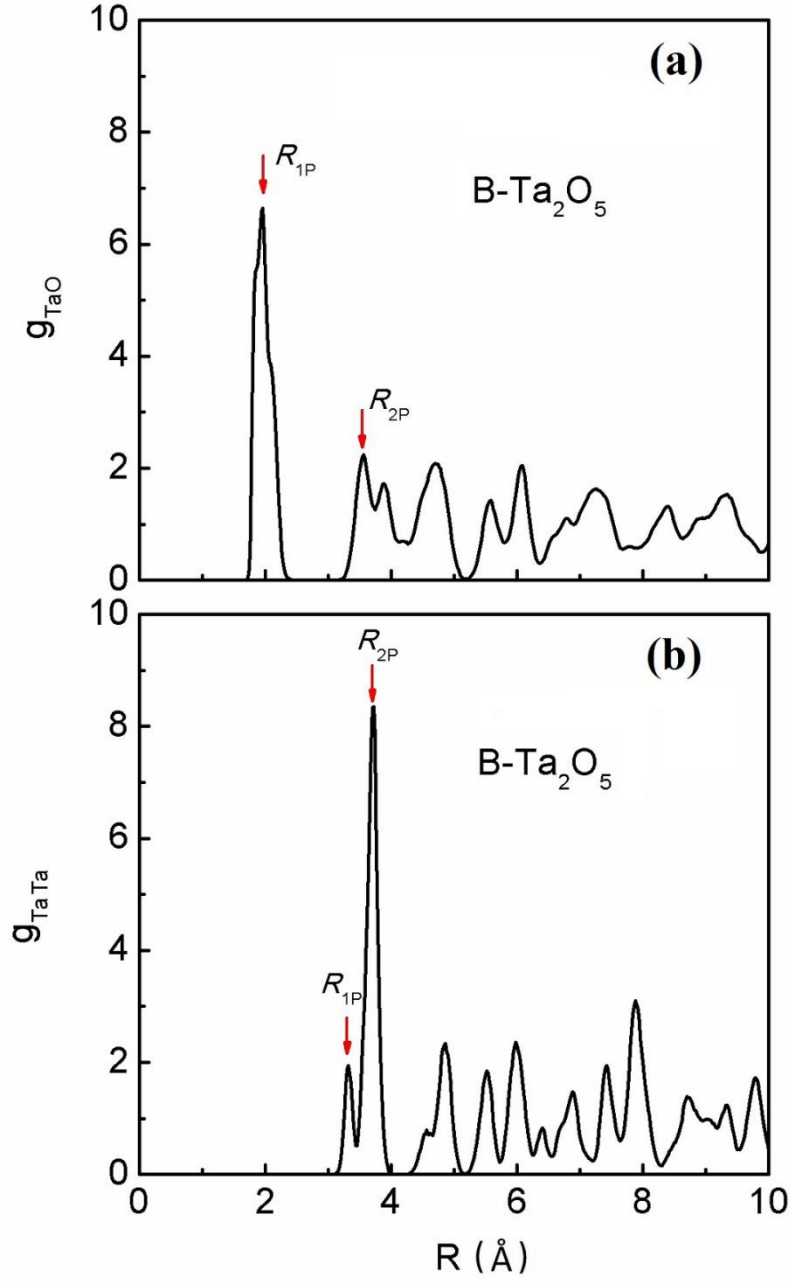


FIG. S3. The radial distribution functions (RDFs) g_{TaO} (a) and g_{TaTa} (b) of B-Ta₂O₅, calculated by averaging over the atomic configurations obtained in MD simulations at 300 K.

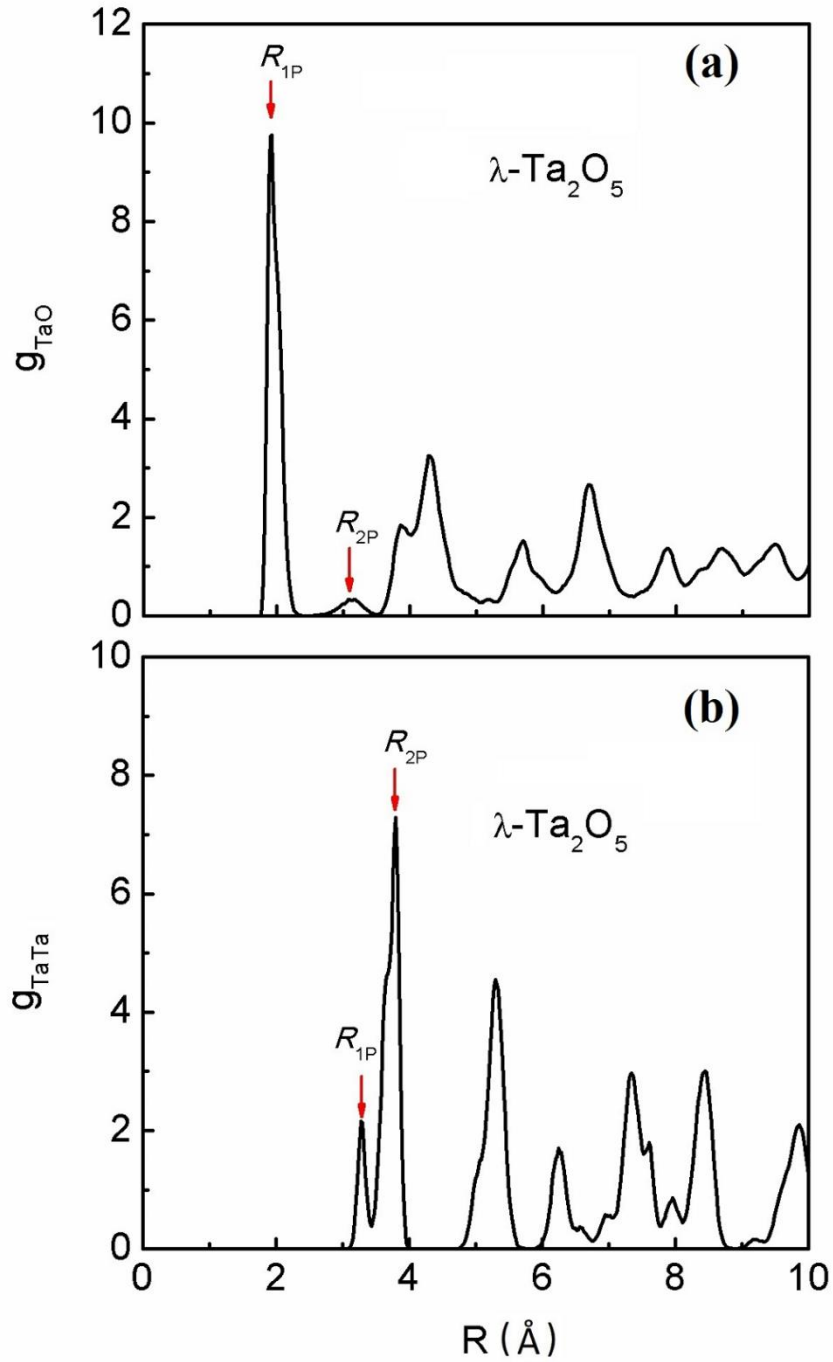


FIG. S4. The RDFs g_{TaO} (a) and g_{TaTa} (b) of λ -Ta₂O₅, calculated by averaging over the atomic configurations obtained in MD simulations at 300 K.

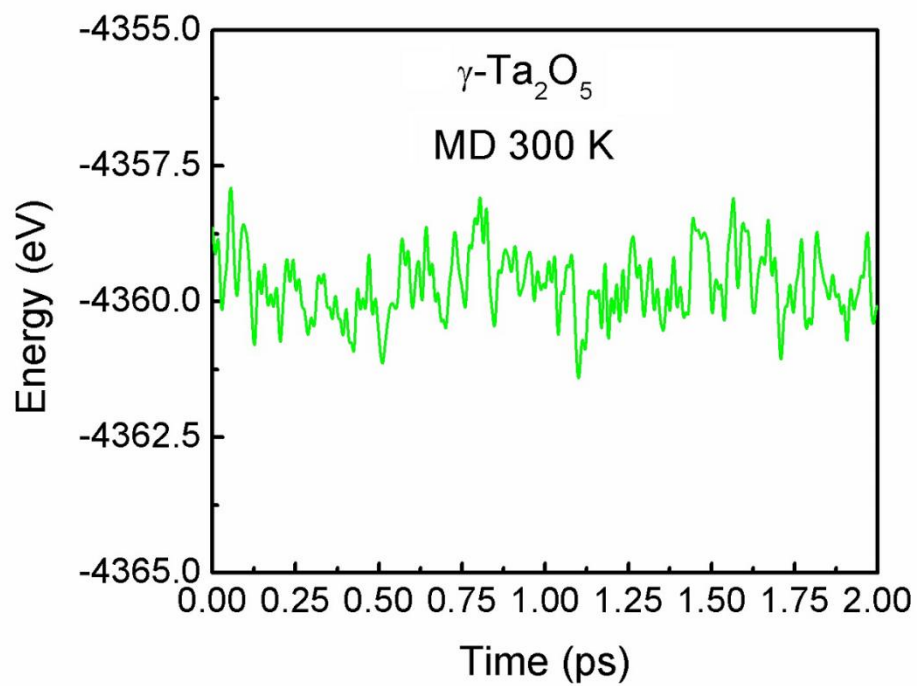


FIG. S5. Total energy of γ -Ta₂O₅ (supercell) as a function of MD simulation time at 300 K.

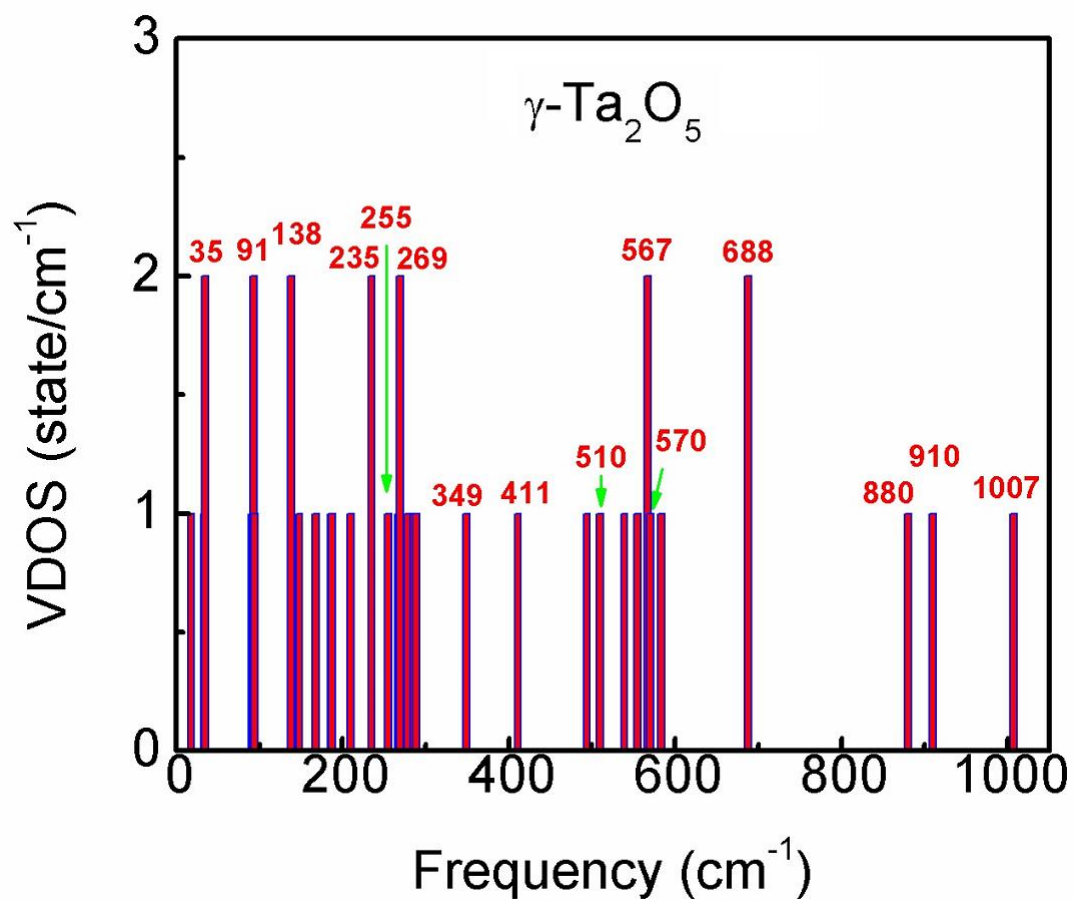


FIG. S6. Calculated phonon vibrational density of states (VDOS) of $\gamma\text{-Ta}_2\text{O}_5$ at Γ -point.

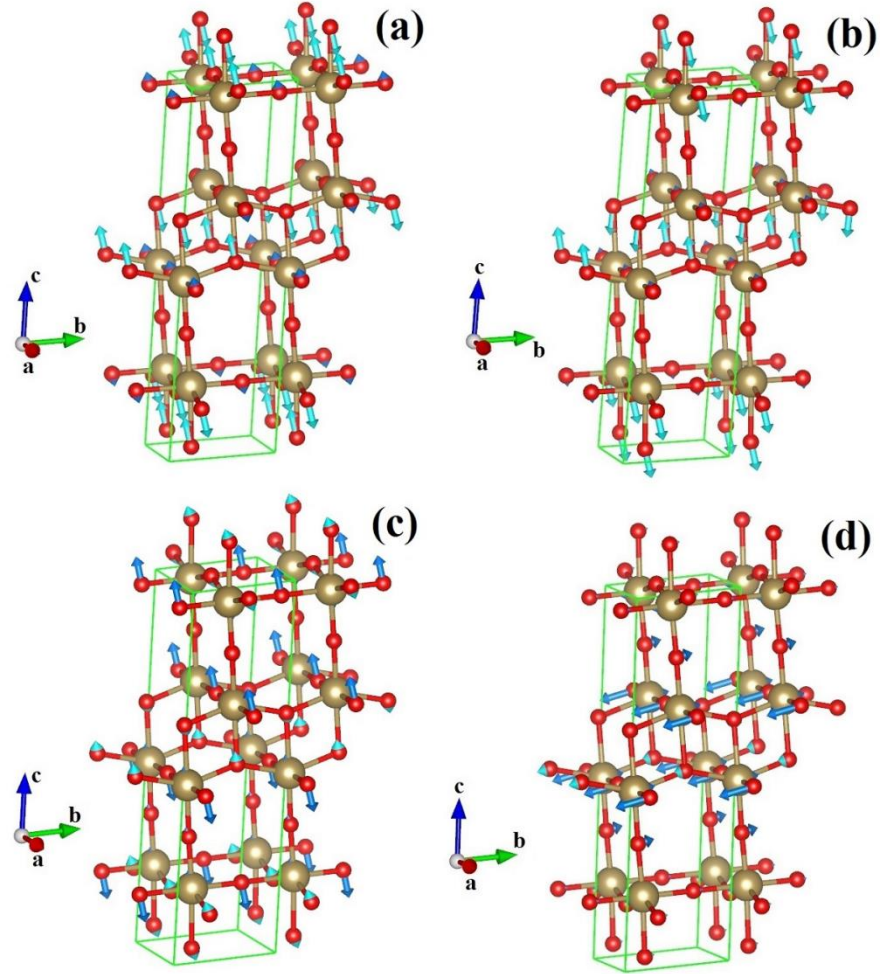


FIG. S7. Polarization vectors of the vibrational modes of γ -Ta₂O₅ at Γ -point with the wave numbers $\tilde{\nu} = 510 \text{ cm}^{-1}$ (a), 570 cm^{-1} (b), 255 cm^{-1} (c), 91 cm^{-1} (d). The vibrations of O_{3c} and O_{2c} are represented by sky-blue and deep-blue arrows, respectively.

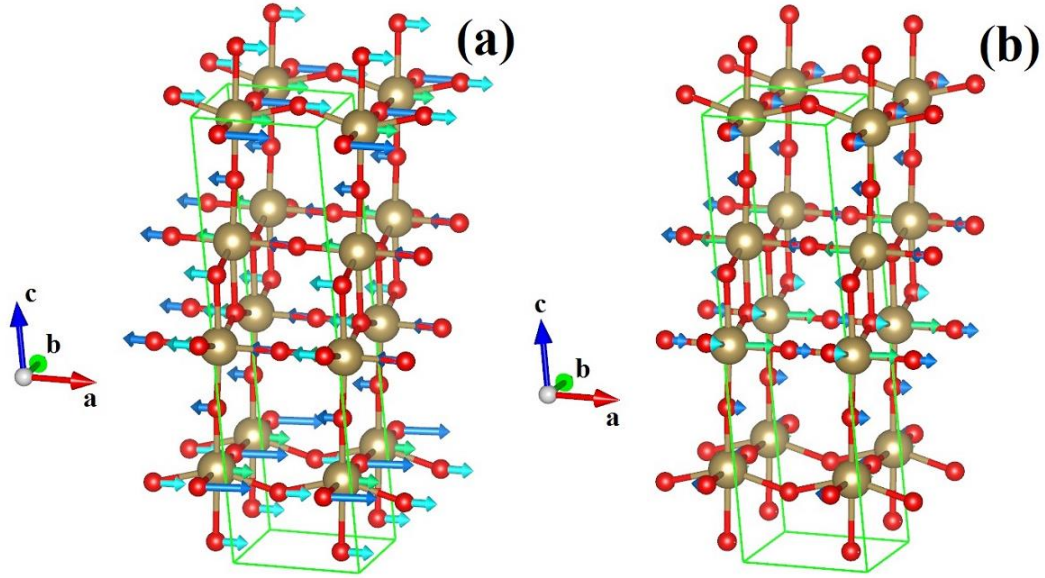


FIG. S8. Polarization vectors of the vibrational modes of γ -Ta₂O₅ at Γ -point with the wave numbers $\tilde{\nu} = 34 \text{ cm}^{-1}$ **(a)**, 35 cm^{-1} **(b)**. The vibrations of O_{3c}, O_{2c} and Ta are represented by sky-blue, deep-blue and green arrows, respectively.

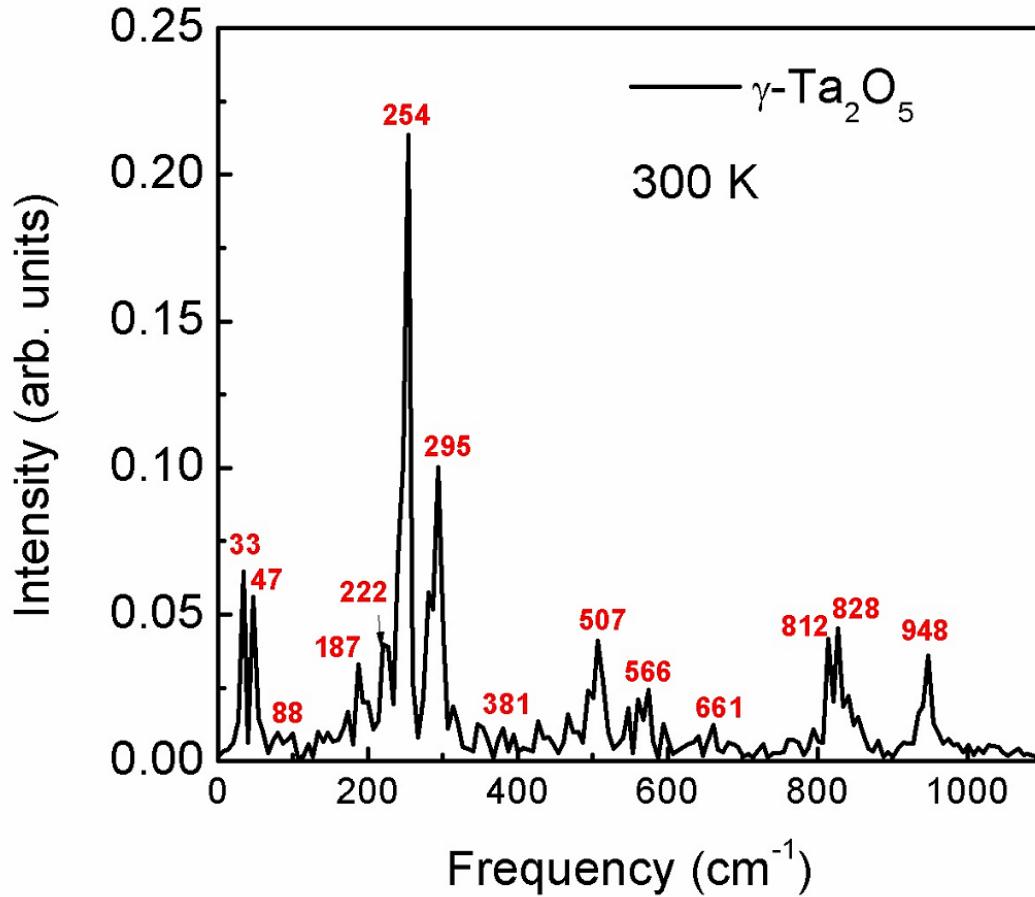


FIG. S9. The vibrational spectrum of γ -Ta₂O₅, calculated from MD simulations at 300 K using the VASP code.

IV. References

- [66] J. P. Perdew and A. Zunger, *Self-interaction correction to density-functional approximations for many-electron systems*. Phys. Rev. B **23**, 5048 (1981).
- [67] S. Nosé *A unified formulation of the constant temperature molecular dynamics methods*. J. Chem. Phys. **81**, 511 (1984).
- [68] S. Nosé *Constant Temperature Molecular-Dynamics Methods*. Prog. Theor. Phys. Suppl. **103**, 1 (1991).
- [69] D. M. Bylander, L. Kleinman, *Energy fluctuations induced by the Nosé thermostat*. Phys. Rev. B **46**, 13756 (1992).